



**HAL**  
open science

## Development of Micromegas detectors with resistive anode pads

M. Chefdeville, R. de Oliveira, C. Drancourt, N. Geffroy, T. Geralis, P. Gkoutoumis, A. Kalamaris, Y. Karyotakis, D. Nikas, F. Peltier, et al.

► **To cite this version:**

M. Chefdeville, R. de Oliveira, C. Drancourt, N. Geffroy, T. Geralis, et al.. Development of Micromegas detectors with resistive anode pads. Nucl.Instrum.Meth.A, 2021, 1003, pp.165268. 10.1016/j.nima.2021.165268 . hal-03217623

**HAL Id: hal-03217623**

**<https://hal.science/hal-03217623>**

Submitted on 24 Apr 2023

**HAL** is a multi-disciplinary open access archive for the deposit and dissemination of scientific research documents, whether they are published or not. The documents may come from teaching and research institutions in France or abroad, or from public or private research centers.

L'archive ouverte pluridisciplinaire **HAL**, est destinée au dépôt et à la diffusion de documents scientifiques de niveau recherche, publiés ou non, émanant des établissements d'enseignement et de recherche français ou étrangers, des laboratoires publics ou privés.



Distributed under a Creative Commons Attribution - NonCommercial 4.0 International License

# Development of Micromegas detectors with resistive anode pads

M. Chefdeville<sup>a,\*</sup>, R. de Oliveira<sup>d</sup>, C. Drancourt<sup>a</sup>, N. Geffroy<sup>a</sup>, T. Geralis<sup>b</sup>,  
A. Kalamaris<sup>b</sup>, Y. Karyotakis<sup>a</sup>, D. Nikas<sup>b</sup>, F. Peltier<sup>a</sup>, O. Pizzirusso<sup>d</sup>,  
A. Psallidas<sup>b</sup>, A. Teixeira<sup>d</sup>, M. Titov<sup>c</sup>, G. Vouters<sup>a</sup>

<sup>a</sup>Univ. Grenoble Alpes, Univ. Savoie Mont Blanc, CNRS, IN2P3-LAPP, Annecy, France

<sup>b</sup>INPP, NCSR Demokritos, Agia Paraskevi, Attiki, Greece

<sup>c</sup>IRFU, Saclay CEA, Gif-sur-Yvette, France

<sup>d</sup>Micro Pattern Technology workshop, DT group, ET department, CERN, Geneva, Switzerland

---

## Abstract

A novel type of resistive Micromegas combining a Bulk mesh and a resistive pad board is presented. Readout pads are covered by a thin insulating layer with a top resistive coating segmented into resistive pads. Readout and resistive pads are electrically connected by means of planar resistors embedded in the insulator, enabling fast clearance of the avalanche charge from the resistive surface. The maximum gas gain achieved by these resistive detectors is similar to that of non-resistive Micromegas. A possible saturation of the gain for large energy deposits in the gas was investigated by means of <sup>55</sup>Fe quanta and electromagnetic showers in the 30–200 GeV energy range, but no significant deviation from a proportional response was found. With a suitable choice of the resistance, these detectors demonstrate negligible gain drop and no sparking up to X-ray fluxes of  $\sim 1 \text{ MHz/mm}^2$  which constitutes a major improvement over non-resistive Micromegas. Spark suppression was also verified in a hadron beam for prototypes with a pad resistance as low as 40 k $\Omega$  or above. Passive protections of the front-end electronics against sparks (diodes on a printed circuit board) are therefore not required for these resistive detectors.

**Keywords:** Micro Pattern Gas Detectors, Micromegas, resistive electrodes

---

\*Corresponding author  
E-mail addresses: [m.chefdeville@lapp.in2p3.fr](mailto:m.chefdeville@lapp.in2p3.fr) (M. Chefdeville)

March 5, 2021

---

29 **1. Introduction**

30 Owing to the small anode-to-cathode distance ( $\sim 100 \mu\text{m}$ ) in Micro Pattern  
31 Gas Detectors (MPGD), the fast removal of positive ions by nearby electrodes  
32 results in a short collection time and eliminates space-charge build-up [1, 2].  
33 MPGDs therefore show excellent rate capability [3] and are good candidates for  
34 experiments at high-luminosity colliders (LC [4, 5, 6, 7], HL-LHC [8], CEPC [9]  
35 and FCC [10]). Occasional sparking could be a serious flaw for such applications  
36 but can be suppressed by means of resistive electrodes. Spark-free operation can  
37 be achieved with different resistive materials (glass, DLC [11, 12]) and detector  
38 designs, most often using a resistive layer but also resistive patterns.

39 In a detector without mechanical imperfections, sparks are triggered by an  
40 ionisation event when the total size in the avalanche exceeds a critical charge  
41 density; this is known as the Raether limit ( $\sim 10^8$  electrons) [13]. It indicates the  
42 transition from avalanche to streamer mode which might occur when too many  
43 primary electrons are released in the gas (by *e.g.* an  $\alpha$ -particle), or when an  
44 electron avalanche generates successor avalanches through feedback mechanisms  
45 [14, 15]. Diverging processes nevertheless, can be impeded by means of resistive  
46 electrodes. Progressive charge-up of the anode by avalanche electrons reduces  
47 locally the electric field and quenches the spark at an early stage of development.  
48 Due to the finite resistivity of the electrode, the surface charge is eventually  
49 drained to ground and the local field is restored after a characteristic time.

50 In a simple detector design, an insulating foil with a resistive surface coating  
51 is coupled to the readout plane. Signal induction is controlled by the electric  
52 properties of the foil and coating, while surface charges are drained to ground  
53 at the edges of the foil where proper connections are made. This grounding  
54 scheme is not suited for large detector sizes and operation at high particle rates

55 due to slow evacuation and pile-up of surface charges and the resulting drop  
56 of gas gain. To mitigate this, a new design using shorter electrical paths to  
57 ground is proposed: the resistive layer is segmented into resistive pads which are  
58 connected to ground by means of resistors embedded in the insulator. Embedded  
59 resistors were initially proposed by de Oliveira *et al.* [16] and first implemented  
60 in COMPASS prototypes using a few mm<sup>2</sup> pads and a relatively large resistance  
61 [17]. More recently and in parallel to this work, prototypes with large pads of  
62  $1 \times 1 \text{ cm}^2$  were studied for the ATLAS experiment [18], where the possibility to  
63 use a continuous resistive coating was also explored [8].

64 In this contribution, small-size prototypes of various pad resistance were  
65 extensively tested. Non-resistive prototypes were also constructed to give a  
66 point of reference. The fabrication process is described in section 2. Results  
67 on gas gain, signal linearity, rate capability and stability to hadrons, which  
68 were partly published in [19], are reported in section 3 to 7. Measurements of  
69 electron showers in a small calorimeter are reported in section 8 where a detailed  
70 simulation model is presented.

71 Larger area prototypes were subsequently built to verify the scalability of  
72 the fabrication process. Their design inherits from previous R&D on Parti-  
73 cle Flow calorimetry where the front-end electronics is integrated directly on  
74 the Bulk Micromegas pad board [5]. Diodes placed between electronic chan-  
75 nel inputs and readout pads absorb the energy of sparks which could otherwise  
76 destroy the sensitive circuits. Three prototypes were equipped with a resistive  
77 Micromegas, including one without diodes to assess the protection capability of  
78 the resistive electrodes itself. A fourth prototype was equipped with an RP-  
79 WELL [7]. Having four detectors, pad-to-pad efficiencies were measured with  
80 an in-situ method. Results are reported in section 9.

81 **2. Detector design**

82 *2.1. Fabrication process*

83 All prototypes are composed of a board with  $1 \times 1 \text{ cm}^2$  pads, a Micromegas  
84 and a resistive stage (Fig.1). The latter is a sandwich of kapton foils and  
85 screen-printed resistive paste and is fabricated as follows. A  $25 \mu\text{m}$  kapton foil  
86 is first glued onto the pad board. Small holes are drilled into the foil and filled  
87 with silver paste to later provide an electrical contact between metallic pads  
88 and embedded resistors. A  $50 \mu\text{m}$  photosensitive film (so-called coverlay) is  
89 then laminated onto the board and etched to the chosen resistor shape (Fig. 2).  
90 Etched spaces are filled with resistive paste by screen-printing. The paste is  
91 baked and its surface polished. A second kapton foil is then glued and drilled  
92 to create the silver vias that will connect resistors to resistive pads. As for  
93 the embedded resistors, a second photosensitive film is used to make resistive  
94 pads (which can themselves be patterned as shown in Fig.3). The shortest  
95 distance between two adjacent resistive pads is  $500 \mu\text{m}$ , resulting in 10 % inactive  
96 regions. After polishing and cleaning, the board is finally equipped with a Bulk  
97 Micromegas [20]. The distance from the anode pad surface to the resistive pad  
98 surface is  $150 \mu\text{m}$  while the amplification gap between the resistive pad and the  
99 mesh is  $128 \mu\text{m}$ .

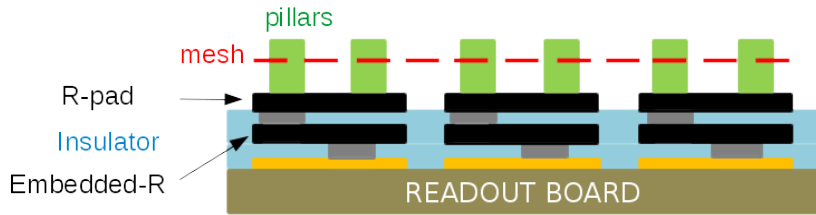


Figure 1: Sketch of Micromegas with embedded resistors (not to scale).

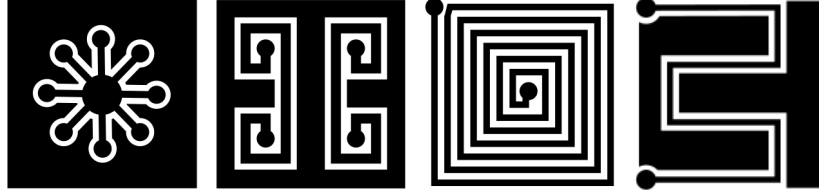


Figure 2: Embedded resistor shapes, from left to right: star, mirror, snake and spider-like patterns. Black spaces are filled with resistive paste, blank spaces with insulating coverlay. Black dots represent vias connecting the embedded resistors to readout or resistive pads.

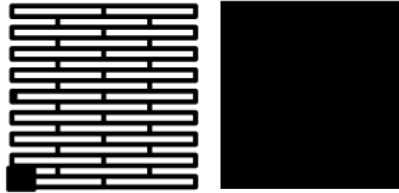


Figure 3: Resistive pad of the spider-like prototype (left) and of other prototypes (right).

100 *2.2. Small prototypes*

101 Small prototypes are built on  $20 \times 30 \text{ cm}^2$  printed circuit boards (PCB). The  
 102 active region is a  $10 \times 10$  matrix of  $1 \times 1 \text{ cm}^2$  copper pads. The four corner pads  
 103 are used to bias the mesh and partly filled with coverlay. The 96 other pads are  
 104 routed to a connector compatible with Gassiplex electronic boards (when anode  
 105 signals are read out) or for direct grounding (when mesh signals are read out).  
 106 In the latter case, signals are digitised by a multi-channel analyser (Amptek's  
 107 MCA-8000D).

108 A first batch of prototypes was produced using a paste with a sheet resistance  
 109  $R_S$  of  $100 \text{ k}\Omega/\square$  (non-resistive prototypes were also produced). After successful  
 110 tests, a second batch with  $R_S = 1 \text{ k}\Omega/\square$  was produced. For a given resistivity,  
 111 the pad-to-ground resistance is given by the shape of the embedded resistor and  
 112 the number of vias (Fig. 1 (bottom)). Vias act as a current divider and influence  
 113 the detector behaviour at high rates. The following designs were studied:

- 114 • *star*: 4 parallel resistors in series with 4 parallel resistors, and 8 vias;

- 115 • *mirror*: 2 parallel resistors and 4 vias;
- 116 • *snake*: one resistor and 2 vias;
- 117 • *spider*: similar to the *snake* pattern but with strip-patterned resistive
- 118 pads.

119 During fabrication, the resistance between top vias and ground was measured  
 120 with an ohmmeter for several pads of the first batch prototypes. A uniformity of  
 121 10 % RMS is achieved. Average values are  $\sim 1, 1.5, 4$  and  $40 \text{ M}\Omega$  for star, spider,  
 122 mirror and snake pattern respectively. Values for the second batch should be  
 123 100 times smaller.

124 Measurements using a GEM foil were performed in a dedicated gas vessel  
 125 where each prototype was successively placed (section 4.1). Later on, the pro-  
 126 totypes were individually equipped with a drift cover in steel, defining a 3 mm  
 127 drift gap. Small openings in this cover serve as X-ray windows. Unless stated  
 128 otherwise, a mixture of Ar/CO<sub>2</sub> 93/7 is flushed through the chambers.

### 129 2.3. Large prototypes

130 Large resistive prototypes are built on  $50 \times 50 \text{ cm}^2$  PCB with anode pads  
 131 on one side and front-end Application Specific Integrated Circuits (ASIC) on  
 132 the other side. This so-called Active Sensor Units (ASU) design developed for  
 133 hadronic calorimetry is described in details in [5]. The rectangular anode pad  
 134 array was changed to a circular array to provide uniform radial containment of  
 135 particle showers. An intermediate board collecting the ASIC data and providing  
 136 high-voltage to the detector was also merged to the ASU. Based on the expe-  
 137 rience with small prototypes, a resistance of  $\sim 1 \text{ M}\Omega$  ( $R_S = 100 \text{ k}\Omega/\square$ ) using a  
 138 snake pattern was chosen for the three large prototypes. A mixture of Ar/CO<sub>2</sub>  
 139 93/7 was used for all tests.

### 140 **3. Gas gain and energy resolution**

#### 141 *3.1. Introduction and calibration*

142 The gas gain of the small prototypes is measured using X-rays from a Cu  
143 target X-ray tube ( $K_\alpha$  line at 8.1 keV). First, the X-ray tube is used to derive  
144 an absolute reference gain  $G_{\text{ref}}$  by measuring the mesh current  $i_{\text{mesh}}$  in the  
145 non-resistive prototype and the photon conversion rate  $f$ :

$$G_{\text{ref}} = \frac{i_{\text{mesh}}}{f N_p q_e} \quad (1)$$

146 where  $N_p$  is the average number of primary electrons released in the gas and  $q_e$   
147 is the electron charge. Next, the relative gain dependence on mesh voltage is  
148 measured by recording the total charge spectrum with the MCA and extracting  
149 the magnitude of the photoelectric peak from a fit. Relative gains are then  
150 converted to absolute gains using  $G_{\text{ref}}$ .

151 As pile-up conditions at mid-range tube power prevent a direct measurement  
152 of the conversion rate, a thin absorber consisting of a copper tape is placed on  
153 the detector window to reduce the rate down a few hundreds of kHz which can  
154 be accurately measured with the MCA. The resulting attenuation determined  
155 as the ratio of mesh currents without and with foil is then used to calculate the  
156 rate without the foil:  $f \sim 56$  MHz.

157 A typical MCA spectrum of X-ray conversions is shown in Fig. 4 where the  
158 photopeak, the escape peak and a bremsstrahlung continuum are visible. After  
159 fitting these contributions to the data points, the ratio  $R$  between the average  
160 ADC value and the most probable ADC value of 0.89 is used to calculate the  
161 average number of primary electrons entering Eq. 1:  $N_p = RE_\alpha/W \sim 268$ ,  
162 where  $E_\alpha \sim 8.1$  keV is the energy of the  $K_\alpha$  line of copper and  $W \sim 26.9$  eV  
163 the mean energy per ion pair in the gas mixture. The average ADC value is  
164 calculated from the fit function to account for events below the MCA threshold.

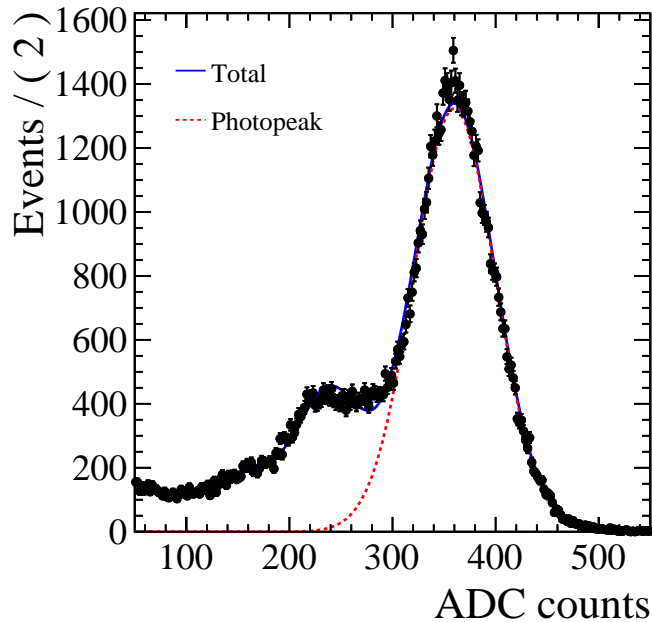


Figure 4: Spectrum of X-ray tube photon conversions measured with a non-resistive prototype. The red-dashed line represents the contribution of the 8.1 keV  $K_{\alpha}$  line of copper, the blue line is the full fit function.

165 *3.2. Gain curves*

166 Gain measurements are performed at a rate of a few kHz. X-rays are colli-  
 167 mated to a 3 mm diameter spot at the centre of a pad such that inactive dielectric  
 168 regions between resistive pads have negligible impact on the measurement. At  
 169 each mesh voltage, the ADC count spectrum is recorded and the gain calculated  
 170 using the previous calibration. Results are summarised in Fig. 5.

171 All prototypes operate at a maximum gain of  $1-2 \cdot 10^4$ . The mesh voltage  
 172 applied to reach a given gain varies by  $\sim 30$  V between the two batches of resis-  
 173 tive prototypes, while the response of the non-resistive prototype, constructed  
 174 first, lies in between. This small dispersion reflects the thickness uniformity  
 175 of the coverlay foils used to make the mesh pillars. Thickness variations from  
 176 different rolls of  $64 \mu\text{m}$  coverlay foils are guaranteed at the  $\pm 7 \mu\text{m}$  level. As

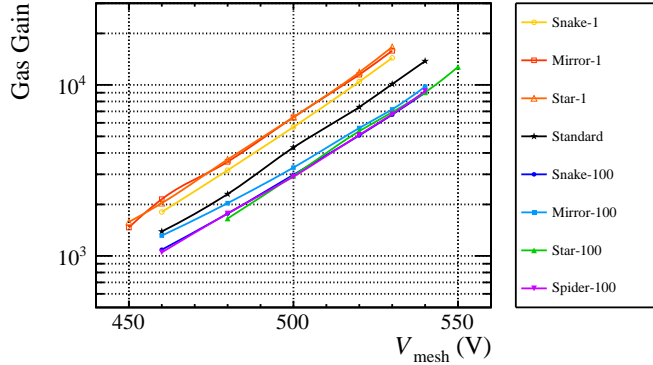


Figure 5: Gas gain versus mesh voltage measured in Ar/CO<sub>2</sub> 93/7 using a Cu target X-ray tube. Measurements with a standard non-resistive prototype are plotted with black star-shaped markers. Other data points correspond to resistive prototypes. The legend indicates the pattern of the embedded resistor (as explained in the article) and its surface resistance (1 kΩ/□ or 100 kΩ/□).

177 two foils are laminated on the pad boards, prototypes from different batches  
 178 can show very different gains. As an example, Monte Carlo simulations of the  
 179 avalanche process in the gas mixture used, predict a relative gain increase of  
 180  $\sim 1.7$  for a  $-14 \mu\text{m}$  variation from a nominal  $128 \mu\text{m}$  thickness [21].

181 Prototypes from the  $100 \text{ k}\Omega/\square$  batch have comparable gas gains. The spectra  
 182 in Fig. 6 also reveal a worse energy resolution (by a factor 2) of the mirror,  
 183 star and spider-like prototypes with respect to the snake-like prototype. The  
 184 latter pattern seems to guarantee superior gap uniformity and achieves 30%  
 185 FWHM, compared to 23% for the non-resistive prototype. A noticeable feature  
 186 in the  $100 \text{ k}\Omega/\square$  prototype distributions is the tail on the right-hand side of the  
 187 photopeak which points to regions of higher gains and therefore poor response  
 188 uniformity. The flatness of the resistive pad surface is indeed crucial to define  
 189 a constant amplification gap and seems to have improved for the second batch  
 190 of prototypes which show an improved energy resolution of about 30% FWHM  
 191 for the three designs, with again best results for the snake-like design.

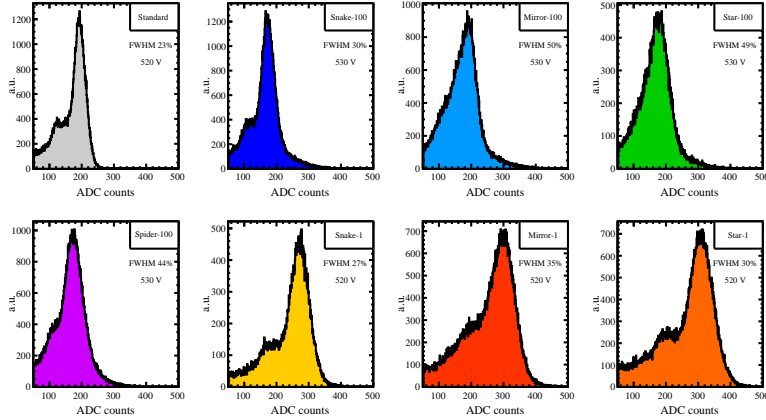


Figure 6: Multi-channel analyser output distributions measured in Ar/CO<sub>2</sub> 93/7 using a Cu target X-ray tube (mesh voltage between 520–530 V).

#### 192 4. Signal linearity with a charge injector

193 Accumulation of electric charge at the surface of the resistive layer can result  
 194 in significant reduction of gas gain. The surface charge distribution reflects the  
 195 arrival of avalanche electrons at the resistive surface which depends on the gas  
 196 gain, event rate and type of ionising radiation (*e.g.* minimum ionising particles,  
 197 X-rays,  $\alpha$ -particles). It is therefore interesting to study the rate dependence of  
 198 the response (in section 5) and if proportionality is preserved at high resistivity  
 199 [22] or high primary charge. Following a setup described in [23], resistive pro-  
 200 totypes are successively tested in combination with a GEM foil that acts as a  
 201 first amplification stage.

##### 202 4.1. Experimental setup

203 A dedicated gas vessel with a kapton-based drift electrode is flushed with  
 204 Ar/CO<sub>2</sub> 90/10. It contains a  $10 \times 10 \text{ cm}^2$  standard GEM foil ( $140 \mu\text{m}$  hole pitch,  
 205  $70 \mu\text{m}$  hole diameter) placed 3 mm above the Bulk mesh to define a 15 mm thick  
 206 drift region. The extraction field is set to 1.3 kV/cm as a balance between  
 207 mesh transparency and GEM extraction efficiency, while a drift voltage of 500 V

208 guarantees a good field uniformity and transmission of electrons through the  
 209 GEM holes. Conversions from 5.9 keV X-rays from a 10 kBq  $^{55}\text{Fe}$  source are  
 210 recorded during two test campaigns (one for each resistivity batch) using the  
 211 same readout as for previous gain measurements.

#### 212 4.2. Calibration of the GEM injector

213 The effective gain is deduced from  $^{55}\text{Fe}$  photon mesh signals at different  
 214 voltages across the GEM electrodes. At  $\Delta V = 0\text{ V}$  across the electrodes, only  
 215 photons converting between the mesh and the GEM are observed: photoelectric  
 216 signals are digitised around position  $p_1$ . Increasing  $\Delta V$ , conversions above the  
 217 GEM are recorded as well and signals are digitised around position  $p_2$ . Fig. 7  
 218 shows a spectrum where the two photon populations are well separated.

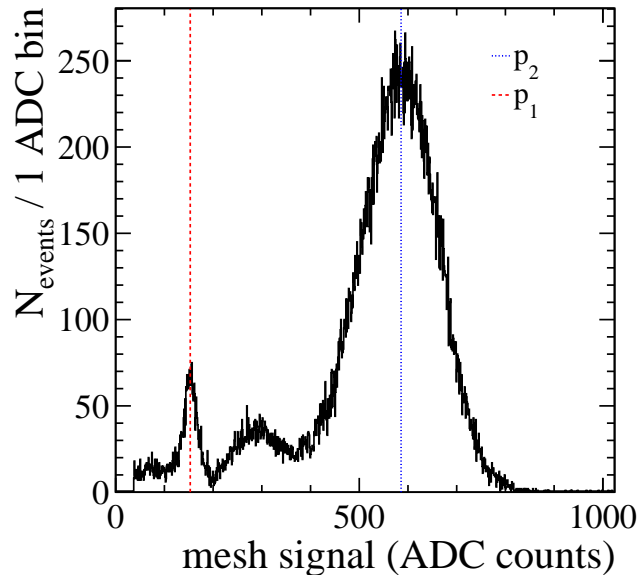


Figure 7: Pulse height histogram when coupling a non-resistive Bulk Micromegas to a GEM pre-amplification stage. The dashed-red line at  $p_1$  corresponds to  $^{55}\text{Fe}$  photons converting between the GEM and the Bulk. The dotted-blue line at  $p_2$  is for conversion above the GEM.

219 The ratio  $p_2/p_1$  should be a direct measure of the effective gain. As shown in  
 220 Fig. 8, effective gains up to several hundreds are achieved. Given the relatively

221 small dynamic range of the preamplifier, the GEM gain had to be measured at  
 222 three different Micromegas gains ( $\sim 10^2$ ,  $10^3$  and  $10^4$  at a mesh voltage of 390,  
 223 460 and 530 V respectively). At decreasing voltages, the Micromegas electron  
 224 collection efficiency is slightly lower. The measurements at 460 and 390 V are  
 225 thus scaled up using the well-known collection curve of the Micromegas (by 8%  
 226 and 22% respectively). Furthermore, the peak position  $p_1$  was only measured  
 227 at 530 V: at lower Micromegas gains, photon conversions above and below the  
 228 GEM can not be separated anymore and  $p_1$  is extrapolated at 460 and 390 V  
 229 using the known slope of the gain curve. The final gain curves of the GEM  
 230 overlap well, as shown in Fig. 8. A slight change of slope is observed which can  
 231 be explained by a more favorable field configuration close to the GEM holes at  
 232 larger  $\Delta V$ .

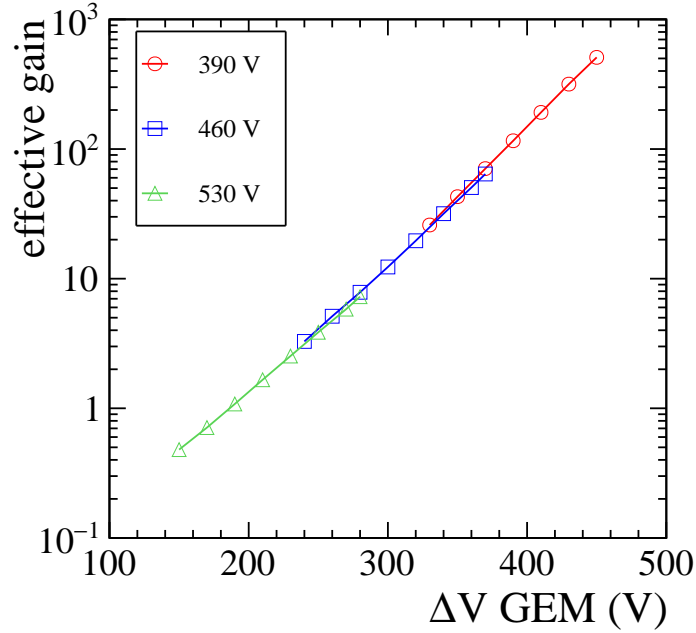


Figure 8: Effective gain of the GEM foil measured at different Micromegas mesh voltages.

### 233 4.3. Response of resistive prototypes

234 The response of resistive prototypes is defined as the  $^{55}\text{Fe}$  photopeak position  
235  $p_2$  as a function of the GEM effective gain from Fig. 8. Prototypes of  $100\text{ k}\Omega/\square$   
236 were operated at gains of  $G \sim 10^2$ ,  $10^3$  and  $10^4$ . Although the charge range is  
237 similar during the three scans, the charge density on the pad surface should be  
238 higher in the last case and could reveal a different behaviour. This is however  
239 not observed and all measured responses are fairly linear over the tested range.  
240 This is illustrated in Fig. 9 where the best straight line fit is added to each  
241 measured response. As opposed to [19] where the straight line was forced to the  
242 origin, the intercept with the vertical axis is now floated to allow for a non-zero  
243 pedestal at the MCA input (this pedestal could not be measured). For a non-  
244 zero pedestal, data points (mainly those with low  $p_2$  values) are shifted from  
245 their true values, yielding a non-physical response. In Fig. 9, points at low  $p_2$   
246 indeed stand below the fit which could, as occurred in [19], be misinterpreted  
247 as saturation.

248 During the second test period, the preamplifier dynamic range was extended  
249 by reducing its gain by a factor 3.5. A single scan was performed for each  $1\text{ k}\Omega/\square$   
250 prototype at a gas gain close to  $10^4$  ( $V_{\text{mesh}} = 510\text{ V}$ ). Response curves are shown  
251 in Fig. 10 and are linear as well, which is compatible with the performance at  
252 higher resistivity.

## 253 5. Rate capability with X-rays

254 Rate capability is a flagship measurement for resistive detectors. It mea-  
255 sures the magnitude of charge-up effects and also offers a ground for testing  
256 spark suppression because overlapping events can be responsible of large primary  
257 charge deposits [24]. Measurements reported in this section were performed first  
258 with the  $100\text{ k}\Omega/\square$  prototypes. When the second batch became available, the

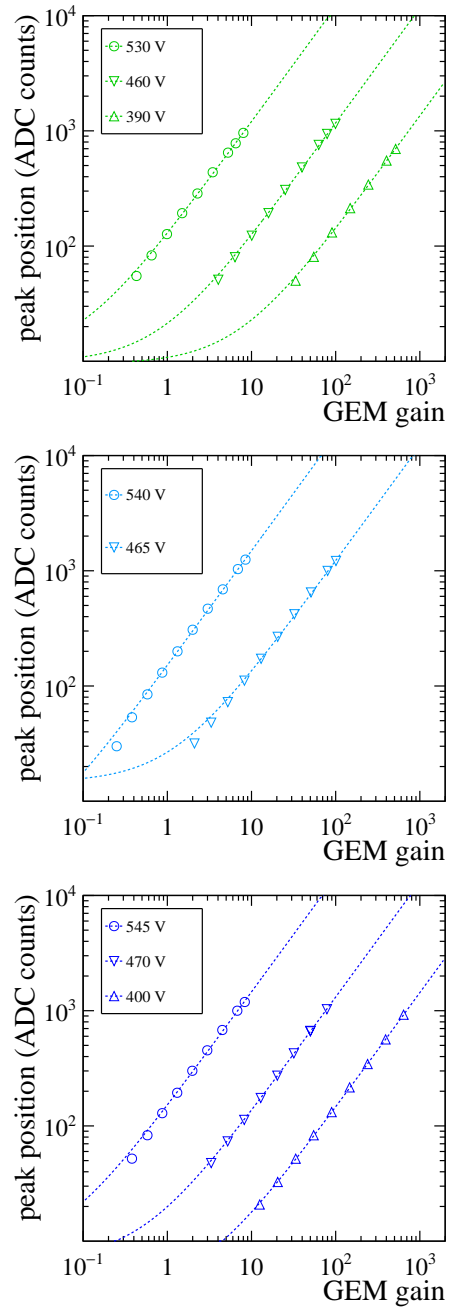


Figure 9: Response of 100 k $\Omega$ / $\square$  resistive prototypes to  $^{55}\text{Fe}$  quanta when using a GEM foil as pre-amplification stage. From top to bottom: star, mirror and snake patterns. Dashed lines are linear functions to guide the eye. The double logarithmic scale is chosen for the sake of readability.

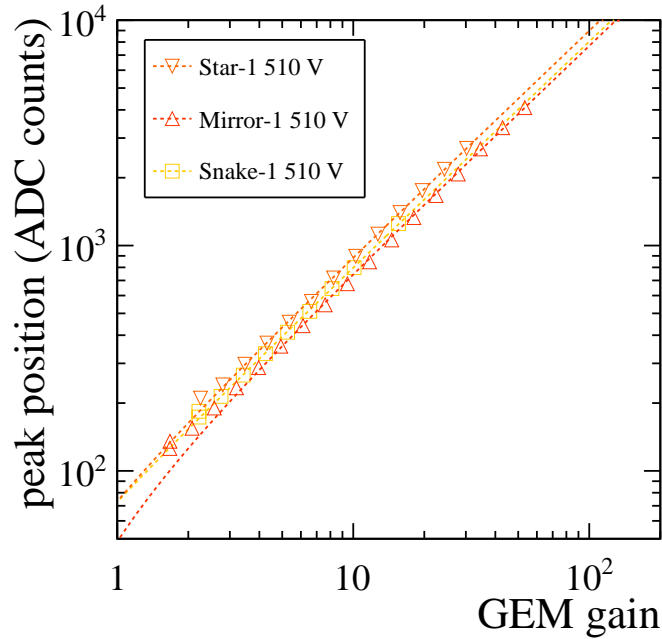


Figure 10: Response of  $1\text{ k}\Omega/\square$  resistive prototypes to  $^{55}\text{Fe}$  quanta when using a GEM foil as pre-amplification stage. Dashed lines are linear functions to guide the eye.

259 measurements were repeated, although at lower rates due to using a different  
 260 apparatus. Results from the two test campaigns are consistent.

### 261 5.1. Experimental setup and protocol

262 The setup is the one used for the gain measurements (section 3). Photons  
 263 from the X-ray tube are collimated to a 3 mm diameter spot at the detector  
 264 window. One pad is illuminated so the current flows through one embedded  
 265 resistor only. Results are easier to interpret this way and charge-up effects are  
 266 maximal. The X-ray tube power is converted into a particle flux using the  
 267 rate calibration of section 3.1 and the known beam spot size. During the first  
 268 test campaign, four rate scans were performed per prototype (at 400, 435, 470,  
 269 505 V). Due to a larger number of prototypes and time constrains in the test  
 270 facility, this was reduced to a single scan during the second campaign.

271 *5.2. First test campaign*

272 Response curves obtained with the 100 k $\Omega$ /□ prototypes are shown in Fig. 11  
 273 where the non-resistive best measurement was added for reference (best meaning  
 274 that sparking was sufficiently rare to measure stable currents). Below 470 V, the  
 275 responses are linear and therefore not shown. At 470 V and 505 V, the response  
 276 of all resistive prototypes saturates. In the absence of saturation, the expected  
 277 gains would be  $\sim 1.5 \cdot 10^3$  and  $\sim 3.5 \cdot 10^3$  respectively. At the highest X-ray tube  
 278 power, the intensity is about 12 MHz/mm<sup>2</sup> and no sparks are observed.

279 At given rate and voltage, prototypes with higher resistance exhibit more  
 280 saturation. For a given prototype, saturation is also more pronounced at high  
 281 rates due to an increased voltage drop across the amplification gap. Ignoring  
 282 space charge effects and charge recombination in the drift region, the current  $i$   
 283 and rate  $f$  are related by:

$$i(f) = i_0(f) \frac{G(f)}{G(0)} = i_0(f) e^{-B\Delta V} = Q_0 f e^{-BRi} \quad (2)$$

284 where  $i_0$  ( $Q_0 = q_e N_p G$ ) is the current (average charge per event) in absence  
 285 of charge-up and is modulated by the gain drop expected from the Ohm's law  
 286 ( $B$  is the slope of the gain curve and  $R$  the pad-to-ground resistance). The  
 287 exponential relation between gain and voltage is used, as measured in Fig. 5.  
 288 For small voltage drops  $\Delta V$ , the exponential can be replaced by its first-order  
 289 Taylor expansion, yielding:

$$i(f) = \frac{Q_0 f}{1 + BRQ_0 f} \quad (3)$$

290 which is valid to a few percent accuracy for  $\Delta V \leq 10 V$  (*i.e.* a gain drop  
 291 below 25%). This assumption should be valid for the star-like and mirror-like  
 292 prototypes for which the parameters  $Q_0$  and  $BR$  can be adjusted to the data.

293 The resulting fits are superimposed on the data points. The expected response  
294 in absence of charge-up is also indicated (numerator of Eq. 3). Deviations from  
295 the linear response are essentially governed by the voltage drop which can be  
296 calculated from the fit parameters. Results are summarised in Fig. 12 where the  
297 voltage drop is plotted against mesh current. Ohm's law is well verified except  
298 for the highest- $R$  prototype (snake pattern) because its expected non-saturated  
299 response can not be precisely derived, Eq. 3 being a poor approximation. In that  
300 case, the non-saturated response is taken from a fit to the lowest voltage data  
301 (400 V) and extrapolated to higher voltages using the known slope of the gain  
302 curve. The limited precision of this extrapolation might explain the departure  
303 from Ohm's law seen in Fig. 12.

### 304 5.3. Second test campaign

305 The X-ray tube power during the second campaign was smaller by a factor  
306 ten. After rate calibration, scans were repeated or performed for the first time.  
307 Repeated measurements are well compatible with those of the first campaign  
308 and labelled as tube2 in Fig. 11. Performance of  $1\text{ k}\Omega/\square$  prototypes measured  
309 at  $\sim 490\text{ V}$  (*i.e.* gas gain of  $\sim 5 \cdot 10^3$ ) are shown in Fig. 13. Only the snake-like  
310 prototype and the  $100\text{ k}\Omega/\square$  spider-like prototype (only tested then) exhibit a  
311 slight saturation due to a higher resistance or operating gain. Despite the low  
312 resistivity used, it is remarkable that stable operation is achieved at such high  
313 rate ( $\sim 1\text{ MHz}/\text{mm}^2$ ) and gas gain.

## 314 6. Discharge rate measurements with X-rays

315 Although sparks were not seen when operating the prototypes in current  
316 mode, a complementary study was performed in pulse mode using a differen-  
317 tiator circuit with a large time constant ( $RC = 0.1\text{ s}$ ) to read out the mesh elec-  
318 trode. The mesh was connected to a  $10\text{ nF}$  capacitor and then a  $10\text{ M}\Omega$  resistor

319 to the ground. The signal was probed from the resistor to a shaper-amplifier  
320 with unit amplification. As verified with Spice software [25], signal frequencies  
321 above 30 Hz are fully transmitted, thus the voltage drop of ionising events can be  
322 recorded by measuring the pulse height. Spectra of voltage drops were recorded  
323 for long periods of irradiation with X-rays (Rh 3 keV X-ray tube) at a high rate  
324 with the spider-like prototype. The Rh X-ray tube operated at 5 kV produces 3  
325 lines of close energies averaging at 2.75 keV. Garfield++ simulation shows that  
326 from each 2.75 keV X-ray absorption in the gas,  $101 \pm 13$  primary electrons are  
327 produced. In order to increase the photon conversion rate a drift gap of 1.4 cm  
328 was used in this setup. The irradiated area was about  $0.18 \text{ cm}^2$  and the observed  
329 currents were up to 90 nA depending on the gain. The detector linearity was  
330 excellent for rates up to tens of  $\text{MHz}/\text{cm}^2$ .

331 Table 1 quotes the maximum voltage drop for gains spanning from  $2\text{--}6 \times 10^3$   
332 at a constant rate of  $11 \text{ MHz}/\text{cm}^2$  over periods of 24 hours. The third column  
333 refers to rates with voltage drop larger than 30 mV, which corresponds to a  
334 charge pulse just above the Raether limit ( $10^8$  electrons), taking into account  
335 the detector capacitance ( $\sim 600 \text{ pF}$ ). The fourth column refers to discharge rates  
336 with voltage drop larger than 0.5 V, corresponding to small but measurable gain  
337 drop. The maximum voltage drop never exceeded 0.8 V for gains up to 4000  
338 while for a gain of 6000 it was at most 2 V with an extreme case of 4.9 V. At  
339 a gain of 2000, no voltage drop greater than 0.5 V was recorded over a period  
340 of 24 hours, corresponding to a relative gain drop below 2% (as deduced from  
341 the slope of the gain curve in Fig. 5). At such rates and gas gains, sparking has  
342 thus a negligible impact on the detector performance.

Table 1: Rates of events provoking a voltage drop larger than 30 mV ( $r_1$ ) and 0.5 V ( $r_2$ ) under 11 MHz/cm<sup>2</sup> X-rays illumination.

Gain	Maximum HV drop (V)	$r_1$ (/cm <sup>2</sup> /s)	$r_2$ (/cm <sup>2</sup> /s)
2000	0.25	$5.5 \times 10^{-4}$	$< 1.3 \times 10^{-4}$
3000	0.80	$1.4 \times 10^{-3}$	$2.8 \times 10^{-4}$
4000	0.80	$2.7 \times 10^{-3}$	$6.8 \times 10^{-4}$
6000	4.90	$1.8 \times 10^{-1}$	$1.4 \times 10^{-1}$

## 343 7. Stability with pion showers

344 Successful operation of resistive prototypes at gains and X-rays fluxes unsus-  
 345 tainable by a standard Micromegas suggests a suppression of sparking already  
 346 at very low resistance values. The charge deposited by X-rays in the gas, how-  
 347 ever, is at most a few hundreds primary electrons. In these conditions, sparks  
 348 mainly occur by superposition in time and space of close-by photon conversions.  
 349 On the other hand, hadrons might release heavily ionising particles with ener-  
 350 gies in the MeV range. Tests with hadrons are therefore necessary to evaluate  
 351 spark suppression in a definitive manner. This is done by scrutinising the mesh  
 352 current during exposure of the detectors to an intense hadron beam at CERN.

### 353 7.1. Experimental setup

354 High-energy 150 GeV/c pions produced in the interaction of the SPS proton  
 355 beam with targets are directed to the North Area of CERN in the H4 beam  
 356 line. The detector stack is composed of nine small Micromegas (seven of which  
 357 are resistive) held perpendicular to the beam direction and biased at 470 V. The  
 358 pion beam has a  $\sim 1 \times 1$  cm<sup>2</sup> transverse size and its rate is about 200 kHz. To  
 359 enhance the number of particles traversing the detector, a  $1.5 \lambda_{\text{int}}$  thick iron  
 360 brick is placed  $\sim 1$  cm upstream of the prototype under test. Mesh and drift  
 361 currents are recorded and analysed offline.

362 *7.2. Results*

363 Typical current recordings from non-resistive and resistive prototypes are  
364 shown in Fig.14. In the first case, the mesh current is quite irregular with  
365 spikes to several  $\mu\text{A}$  interpreted as frequent sparking. On the other hand, most  
366 resistive prototypes show reduced and stable currents which can be explained  
367 as an absence of sparking.

368 Currents at the highest pion rate are binned into histograms to make an  
369 easier comparison. Histograms are plotted in Fig.15. Except for the lowest  
370 resistance prototype, mesh currents are roughly constant: current distributions  
371 show a peak at  $\sim 200\text{ nA}$  and  $\sim 500\text{ nA}$  for the  $100$  and  $1\text{ k}\Omega/\square$  prototypes re-  
372 spectively. The current ratio between the two resistivity values is consistent  
373 with the known gain curves. Interestingly, the behaviours of the lowest re-  
374 sistance prototype and standard Micromegas are similar, which suggests that  
375 sparks are suppressed if the resistance is larger than a threshold value.

376 The physical meaning of this threshold resistance is unknown. As an out-  
377 look to future investigations, we propose that it reflects a competition between  
378 the physical processes that charge-up the resistive elements (avalanche growth)  
379 and those that discharge it (RC constant). If the electric field is restored too  
380 quickly, electron avalanches can diverge and lead to a spark. If not, charges  
381 pile-up and quench the spark by local reduction of the electric field. In this  
382 model, sparks are suppressed if the RC constant is larger than the timescale  
383 of the avalanche development ( $\sim 1\text{ ns}$ ). Examination of the validity of this  
384 model involve measurement and modelling of the time response of the resistive  
385 detectors and should be part of future work.

## 386 8. Response to electromagnetic showers

387 Modelling and measuring the detector response and scrutinizing the level  
388 of agreement between them offers a ground for testing the understanding of  
389 the underlying physical processes. This approach is followed using electrons in  
390 the 30–200 GeV range showering in a small calorimeter of six prototypes (two  
391 standard and four resistive) and iron absorbers. The total charge per shower is  
392 measured at different energies and compared to simulation. All prototypes are  
393 simulated nearly in the same way (*i.e.* the resistive layer is ignored) except for  
394 variations in average gas gain. As will be shown, this approximation is good  
395 enough to reproduce the data.

### 396 8.1. Experimental setup

397 Four  $100\text{ k}\Omega/\square$  resistive prototypes and two non-resistive prototypes from  
398 the SPS/H4 setup described in section 7 were used. Adding iron absorbers  
399 between the prototypes (Fig. 16), a calorimeter thickness equivalent to  $\sim 23 X_0$   
400 and  $\sim 2.4 \lambda_{\text{int}}$  is achieved which is sufficient to contain the electron showers.

401 Individual pads are read out by Gassiplex electronics upon reception of a  
402 scintillator trigger and digitised with 10-bits resolution (see [26] for details). A  
403 working voltage of 470 V was chosen as a compromise between high signal-over-  
404 noise ratio and rare ADC saturation. The beam was set at six energy points  
405 (30, 50, 70, 90, 130 and 200 GeV) with almost constant transverse size and rate  
406 ( $\sim 1 \times 1\text{ cm}^2$  and 1–2 kHz). Its composition is energy-dependent with *e.g.* a  
407 pion fraction of 30 % at 200 GeV. This contamination is reduced offline using  
408 the first calorimeter layer as a preshower. About  $5 \times 10^4$  events were recorded  
409 at each energy.

410 *8.2. Simulation*

411 The Monte Carlo (MC) Geant4 software toolkit (version 10.5, [27]) is used  
412 to model the calorimeter and simulate the development of showers (the beam  
413 line instrumentation is ignored). Geant4 energy deposits in the gas are digitised  
414 by a standalone program which shifts and smears the beam position. Primary  
415 electrons are generated according to the  $W$  value of the gas mixture. The  
416 avalanche process is using the individual gas gains of section 3, assuming expo-  
417 nential fluctuations. Next, the number of electrons to ADC counts conversion  
418 is performed using the electronic gain from the Gassiplex data-sheet. Measured  
419 pedestals are subtracted from the ADC counts. If the difference is above  $2^{10}$ ,  
420 the ADC value is set to 1024 to reflect the dynamic range of the ADCs. Finally,  
421 the event reconstruction proceeds the same for simulated and real data. For  
422 each detector channel, the ADC value is compared to a threshold equal to ten  
423 times the pedestal noise. A signal above threshold is counted as a hit.

424 Electrons and pions samples are generated at each energy point. Pion sam-  
425 ples serve the definition of various cuts applied to real data to improve the  
426 electron purity. For this purpose,  $10^4$  pion events per energy point are suf-  
427 ficient. To align with the statistics in real data,  $4 \times 10^4$  electron events are  
428 simulated at each energy.

429 *8.3. Event selection and charge fits*

430 Electrons and hadrons leave different signature in the calorimeter. Pions  
431 traversing the calorimeter without showering leave roughly one hit per layer  
432 and are easily identified. Late-showering pions can be suppressed using the  
433 energy-weighted barycentre along the beam direction which is relatively small  
434 for electrons. Larger fluctuations in the transverse development of pion showers  
435 provide additional handles. To reduce lateral energy leakage, fiducial cuts on  
436 the horizontal and vertical barycentres are also applied. Cut values are deduced

437 from simulation. Selection efficiencies are about 95 % for electrons and 14 % for  
 438 pions (Table 2).

$E_{\text{beam}}$ (GeV)	30	50	70	90	140	200
$\epsilon_{e^-}$ (%)	95.1	94.6	93.4	93.4	96.0	96.0
$\epsilon_{\pi^-}$ (%)	15.8	14.8	13.0	12.9	14.5	15.5
$N_e \times 10^{-3}$	37	35	30	25	33	26
$(\mu_{\text{data}} - \mu_{\text{MC}})/\mu_{\text{MC}}$ (%)	-2.0	5.2	-0.7	1.1	-0.2	-3.4
$R_{\text{data}} - R_{\text{MC}}$ (%)	1.3	0.5	1.1	0.7	0.6	0.6

Table 2: Expected selection efficiency for electrons and pions versus energy. The fourth row indicates the number of selected electron events in the data. Data/MC agreement for the average charge ( $\mu$ ) and resolution ( $R$ ) is indicated in the last two rows.

#### 439 8.4. Results

440 Total charge distributions after selections are shown in Fig. 17 where the  
 441 MC distributions are scaled to the data statistics. A good overall agreement is  
 442 found. Calorimeter performances are fitted to the data points. Since electron  
 443 samples are very pure, their charge distribution is modelled by a Novosibirsk  
 444 function (defined in Appendix A) to account for an eventual radiative tail. The  
 445 electron response shown in Fig. 18 (top) is the relation between the mean total  
 446 charge  $\mu$  and the electron energy. Charge resolution calculated as  $\sigma/\mu$  improves  
 447 with energy (Fig. 18 (bottom)) as expected from the stochastic fluctuations of  
 448 the shower process. Simulation results are included in the figures. The MC  
 449 response agrees with data at the  $\sim 5\%$  level (Table 2) while simulated charge  
 450 distributions are always slightly narrower. A small offset of 1 % in data might  
 451 be due to pad-to-pad gas gain variations which are not modelled. The overall  
 452 scale and trend are nevertheless well reproduced and no striking features from  
 453 using resistive Micromegas are observed.

## 454 **9. Large resistive prototypes**

455       Following a detailed exploration of the parameter space of small prototypes,  
456 three prototypes of larger size ( $\sim 0.2 \text{ m}^2$ ) using snake-like embedded resistors  
457 ( $R = 1 \text{ M}\Omega$  with  $R_S = 100 \text{ k}\Omega/\square$ ) were constructed and tested to demonstrate  
458 that the manufacturing process can be used for larger PCBs. Two of them are  
459 equipped with diodes to protect the front-end electronics against discharges.  
460 The third prototype features only the resistive electrodes to ultimately test the  
461 suppression of sparks for this type of resistive Micromegas.

### 462 *9.1. Resistive Active Sensor Units and test setup*

463       Compact detector designs for sampling calorimetry at a future  $e^+e^-$  linear  
464 collider are studied by the CALICE collaboration. In these designs, the front-  
465 end electronics and the sensitive medium are held on a same support (a PCB)  
466 to allow for very-high granularity. A Micromegas design was proposed and  
467 studied using  $1 \times 1 \text{ m}^2$  prototypes, each composed of so-called Active Sensor  
468 Units (or ASU) placed inside a common gas vessel [5]. The ASU consisted of a  
469 Bulk Micromegas laminated on a 1.2 mm thin PCB with pads on one side and  
470 diode-protected front-end chips (or ASICs) on the other side. This detector was  
471 not resistive and subject to sparking [28]. A natural evolution was to make it  
472 resistive. The resistive ASUs are equipped with 1792 readout pads forming a  
473 circular active area which reflects the rotational symmetry of hadron showers.

### 474 *9.2. MIP efficiency and spatial uniformity*

475       Given the 20-fold increase of the active area, emphasis was first put on  
476 characterising the uniformity of the response by means of a wide 150 GeV muon  
477 beam (SPS/H4 beam line). Composed of three resistive Micromegas ASU and  
478 a fourth ASU equipped with a large RPWELL electrode [7], the detector stack  
479 can be used to measure hit efficiency without external information thanks to a

480 common data acquisition system. The efficiency plateau is first measured locally  
481 for one prototype to define a working voltage. The detector stack is then moved  
482 horizontally and vertically across the beam at constant voltage to control the  
483 uniformity of the response over most of the pads.

484 Muon trajectories are reconstructed using the time and position of hits in  
485 three so-called telescope prototypes: single hits with same pad coordinates and  
486 timestamp are required. The efficiency of the fourth test prototype is inferred  
487 from the presence of a hit in a small time and space interval around the expected  
488 coordinates ( $\pm 200$  ns and  $\pm 1$  pad). Fig. 20 shows the trend of efficiency together  
489 with a previous measurement performed with a  $1 \times 1$  m<sup>2</sup> non-resistive prototype  
490 using a different argon-based mixture [5]. The plateau is reached at a different  
491 voltage as expected, but the resistive ASU achieves a slightly inferior efficiency  
492 by 2–3%. Inactive dielectric regions between resistive pads could explain this  
493 drop. Although mitigated by the transverse diffusion of the electrons in the drift  
494 region and not relevant for calorimeter resolution, this effect could be reduced  
495 in a future design with wider resistive pads.

496 Fig. 21 shows two-dimensional efficiency maps obtained at 500 V where the  
497 statistical error per pad is below 1.5%. Most probable value and dispersion  
498 calculated from a binned fit to the 1D-distributions are listed in Table 3. The  
499 measured dispersion is comparable to the statistical error, meaning that it is  
500 not significant. To assess the systematic error arising from the size of the search  
501 region, the analysis was repeated with larger window sizes, up to  $\pm 7$  pads.  
502 In that last case, the most probable efficiency increased by  $\sim 0.2\%$  suggesting  
503 that the measurement is robust against noise. If we ignore the data points  
504 corresponding to one wrongly configured ASIC, the uniformity is thus given by  
505 the statistical error, *i.e.* better than 2%.

Prototype	#1	#2	#3
$\epsilon_\mu$ (%)	95.6	92.7	97.4
RMS( $\epsilon_\mu$ ) (%)	1.5	1.1	1.0
$\Delta_\epsilon$ (%)	0.1	0.3	0.1

Table 3: Most probable muon efficiency  $\epsilon_\mu$  measured over the prototype active region using a  $\pm 1$  pad search region and its standard deviation RMS( $\epsilon_\mu$ ). The last row reports the efficiency shift  $\Delta_\epsilon$  when using a  $\pm 7$  pads search region.

506 *9.3. Stability in a high-intensity pion beam*

507 Detector stability was then studied using a pion beam collimated to a nar-  
508 row region at the detectors. From the measured beam profile, an intensity of  
509  $\sim 0.5$  MHz/cm<sup>2</sup> is estimated at the central pad. The mesh voltages of the Mi-  
510 cromegas prototypes are raised from 430 V to 540 V in eight increments and the  
511 data acquisition system is kept running during the scan. At each voltage in-  
512 crement, the integrity of the front-end electronics is checked by configuring the  
513 ASICs and scrutinising the reconstructed beam profile.

514 Variations of mesh currents are recorded by the RD51 slow-control system (  
515 Fig. 22). At a given voltage, all mesh currents are roughly constant during the  
516 spills. At equal voltages, larger currents are measured in downstream prototypes  
517 due to an increased particle multiplicity along the beam direction when pion  
518 shower inside the detector material. All prototypes operate up to the highest  
519 tested voltage value which should correspond to a gain of  $10^4$  as charge-up  
520 effects are small ( $\Delta V \sim 1$  V). Most importantly, their behavior are similar and  
521 no damage to the readout electronics was observed. The resistive layer solely  
522 protects the electronics against sparking and could therefore replace the PCB  
523 diode networks in this function. The possible simplification of the PCB design  
524 is an important finding in view of a large-scale application at a future physics  
525 experiment as both high performance and cost effectiveness are desirable.

526 **10. Conclusions**

527 Embedded resistors are an interesting evolution of resistive layers to im-  
528 prove the rate capability of gas detectors by using a shorter electrical path to  
529 ground. Combined with a Bulk Micromegas, they suppress sparking already at  
530 surprisingly low values of resistivity ( $1 \text{ k}\Omega/\square$ ) for which charge-up effects have  
531 negligible impact on the detector response, even at very high rates or for large  
532 energy deposits. Cross-talk from charge diffusion over the resistive surface can  
533 be avoided by segmentation of the layer into resistive pads, at the cost of a few  
534 percent loss of MIP efficiency in the studied designs. An important limitation  
535 of resistive MPGD is hence lifted as the electric path from pad to ground does  
536 not scale with the detector size anymore, which in principle paves the way to  
537 the construction of arbitrary large resistive detectors. As a first step in this  
538 direction, resistive prototypes of moderate size ( $\sim 0.2 \text{ m}^2$ ) were successfully  
539 constructed and operated with high MIP efficiency (95%), excellent uniformity  
540 (below 2%) and no sparks. Replacement of conventional ASIC protection diodes  
541 by embedded resistors is also an important finding which should simplify the  
542 construction of larger detectors and lower their cost.

543 **Appendix A. Fit functions**

544 The Novosibirsk function is given by

$$f(x; \mu, \sigma, t) = \exp \frac{-\ln^2(1 + t\Lambda \frac{x-\mu}{\sigma})}{2t^2} - \frac{t^2}{2} \quad (\text{A.1})$$

545 where  $\Lambda = \sinh t\sqrt{\ln 4}/(t\sqrt{\ln 4})$ . This function approaches a Gaussian function  
546 when the parameter  $t$  vanishes.

547 **Acknowledgements**

548 This work has been partially supported by the RD51 common project SCREAM.  
549 Several studies reported in this paper were made using the collaboration infras-  
550 tructures and hardware. The authors are grateful to the RD51 collaboration  
551 for its decisive support. This research was supported in part by the Grant  
552 No 5029538 from the Structural Funds, European Regional Development Funds  
553 (ERDF) and European Structural Funds (ESF), Greece.

554 **References**

555 **References**

- 556 [1] Y. Giomataris et al. MICROMEGAS: A High granularity position sensitive  
557 gaseous detector for high particle flux environments. *Nucl. Instrum. Meth.*,  
558 A376:29–35, 1996.
- 559 [2] F. Sauli. GEM: A new concept for electron amplification in gas detectors.  
560 *Nucl. Instrum. Meth.*, A386:531–534, 1997.
- 561 [3] M. Titov and L. Ropelewski. Micro-pattern gaseous detector technologies  
562 and RD51 Collaboration. *Mod.Phys.Lett.*, A28:1340022, 2013.
- 563 [4] D.C. Arogancia et al. Study in a beam test of the resolution of a Micromegas  
564 TPC with standard readout pads. *Nucl. Instrum. Meth.*, A602:403–414,  
565 2009.
- 566 [5] C. Adloff et al. Construction and test of a  $1 \times 1 m^2$  Micromegas chamber  
567 for sampling hadron calorimetry at future lepton colliders. *Nucl. Instrum.*  
568 *Meth. A*, 729:90–101, 2013.
- 569 [6] A. White. Development of GEM-based Digital Hadron Calorimetry using  
570 the SLAC KP1X chip. *JINST*, 5:P01005, 2010.

- 571 [7] S. Bressler et al. Novel Resistive-Plate WELL sampling element for  
572 (S)DHCAL. *Nucl. Instrum. Meth.*, A951:162861, 2020.
- 573 [8] T. Alexopoulos et al. A spark-resistant bulk-micromegas chamber for high-  
574 rate applications. *Nucl. Instrum. Meth.*, A640:110–118, 2011.
- 575 [9] The CEPC Study Group. CEPC Conceptual Design Report, Volume 2.  
576 *ArXiv e-prints*, 1811.10545, 2019.
- 577 [10] A. Abada et al. FCC-ee: The Lepton Collider Future Circular Collider Con-  
578 ceptual Design Report, Volume 2. *The European Physical Journal Special*  
579 *Topics*, 228:261–623, 2019.
- 580 [11] G. Bencivenni et al. The  $\mu$ -RWELL layouts for high particle rate. *JINST*,  
581 14(5):P05014, 2019.
- 582 [12] F. Yamane et al. Development of the Micro Pixel Chamber with DLC  
583 cathodes. *Nucl. Instrum. Meth.*, A951:162938, 2020.
- 584 [13] H. Raether. *Electron avalanches and breakdown in gases*. Butterworths  
585 advanced physics series. London, Butterworths, 1964.
- 586 [14] V. Peskov et al. Feedback and breakdowns in microstrip gas counters. *Nucl.*  
587 *Instrum. Meth.*, A397:243–260, 1997.
- 588 [15] Yu. Ivanyushenkov et al. Breakdown limit studies in high-rate gaseous  
589 detectors. *Nucl. Instrum. Meth.*, A422:300–304, 1999.
- 590 [16] R. Oliveira. Resistive protections for Bulk Micromegas, Talk given at the  
591 5<sup>th</sup> RD51 Collaboration Meeting, Freiburg, Germany, May 24-27,2010.
- 592 [17] D. Neyret et al. New pixelized Micromegas detector with low discharge  
593 rate for the COMPASS experiment. *JINST*, 7:C03006, 2012.

- 594 [18] M. Alviggi et al. Construction and test of a small-pad resistive Micromegas  
595 prototype. *JINST*, 13(11):P11019, 2018.
- 596 [19] M. Chefdeville, Y. Karyotakis, T. Geralis, and M. Titov. Resistive Mi-  
597 cromegas for sampling calorimetry, a study of charge-up effects. *Nucl.*  
598 *Instrum. Meth. A*, 824:510–511, 2016.
- 599 [20] Y. Giomataris et al. Micromegas in a bulk. *Nucl. Instrum. Meth.*,  
600 A560:405–408, 2006.
- 601 [21] Georgios Iakovidis. *Research and Development in Micromegas Detector for*  
602 *the ATLAS Upgrade*. PhD thesis, Natl. Tech. U., Athens, 10 2014. CERN-  
603 THESIS-2014-148.
- 604 [22] A. Rubin et al. First studies with the Resistive-Plate WELL gaseous mul-  
605 tiplier. *JINST*, 8:P11004, 2013.
- 606 [23] S. Bressler, L. Moleri, L. Arazi, E. Erdal, A. Rubin, M. Pitt, and A. Bre-  
607 skin. A concept for laboratory studies of radiation detectors over a broad  
608 dynamic-range: instabilities evaluation in THGEM-structures. *JINST*,  
609 9:P03005, 2014.
- 610 [24] V. Peskov and P. Fonte. Research on discharges in micropattern and small  
611 gap gaseous detectors. *arXiv*, physics.ins-det, 0911.0463.
- 612 [25] L.W. Nagel and D. O. Pederson. Simulation Program with Integrated Cir-  
613 cuit Emphasis - SPICE. *Univeristy of California, Berkeley*, Memorandum  
614 No. ERL-M382, Apr. 1973.
- 615 [26] C. Adloff et al. MICROMEAS chambers for hadronic calorimetry at a  
616 future linear collider. *JINST*, 4:P11023, 2009.
- 617 [27] S. Agostinelli et al. GEANT4: A Simulation toolkit. *Nucl. Instrum. Meth.*  
618 *A*, 506:250–303, 2003.

619 [28] C. Adloff et al. Test in a beam of large-area Micromegas chambers for  
620 sampling calorimetry. *Nucl. Instrum. Meth. A*, 763:221–231, 2014.

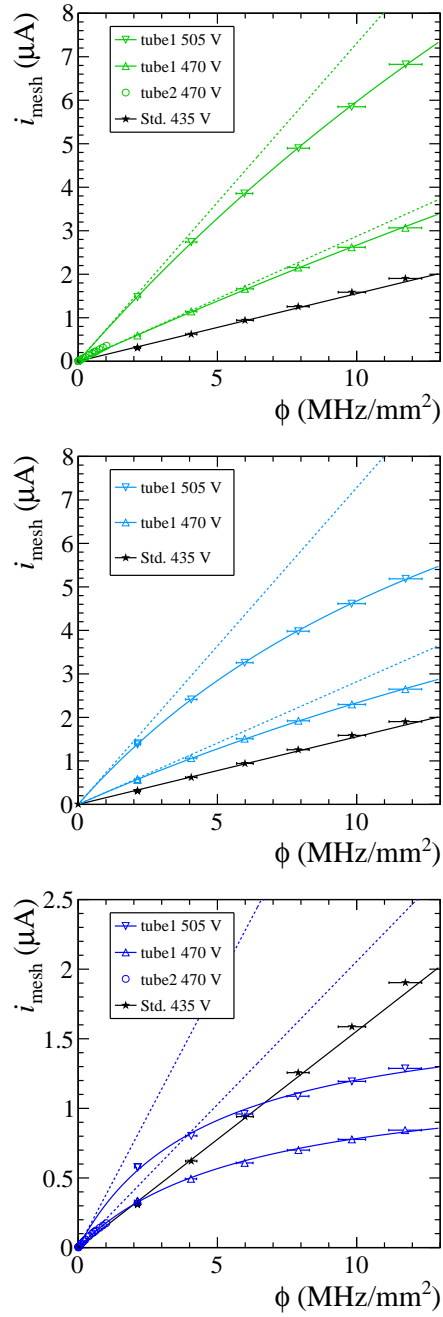


Figure 11: Rate capability of  $100\text{ k}\Omega/\square$  resistive prototypes. From top to bottom: star, mirror and snake-like resistor pattern. Plain lines are a fit of Eq.3 to the data points and dashed lines are the expected response in absence of charge-up. Points and lines in black color are the best measurement performed with a standard non-resistive prototype.

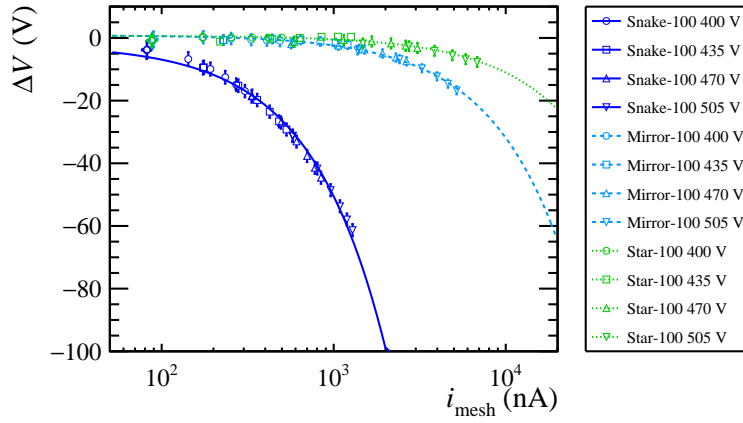


Figure 12: Rate capability of  $100\text{ k}\Omega/\square$  resistive prototypes plotted as a voltage to current dependence. Markers are data points. Lines are a fits of a linear function to the data and represent Ohm's law.

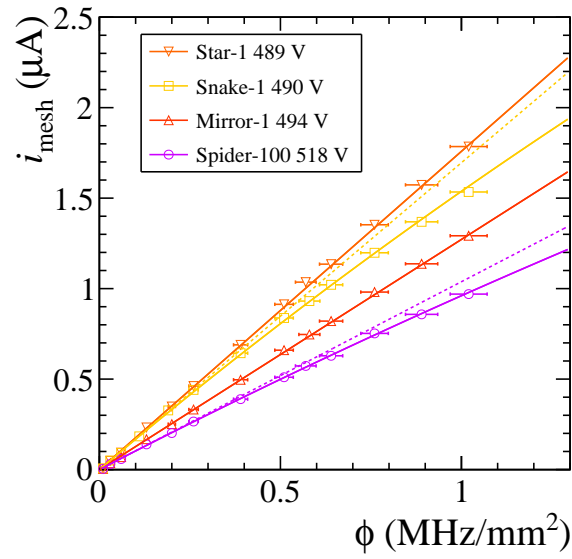


Figure 13: Rate capability of  $1\text{ k}\Omega/\square$  resistive prototypes. Plain lines are the fits of Eq. 3 to the data points and dashed lines are the expected response in absence of charge-up.

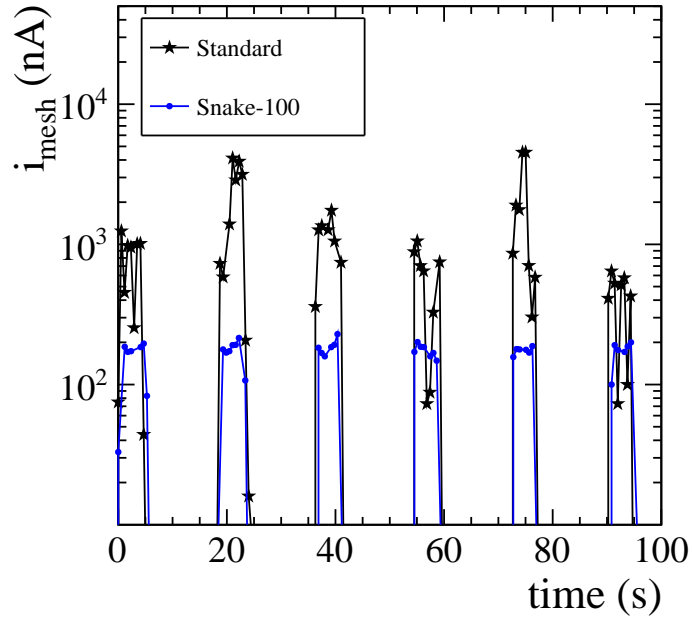


Figure 14: Mesh current under periodic pion irradiation.

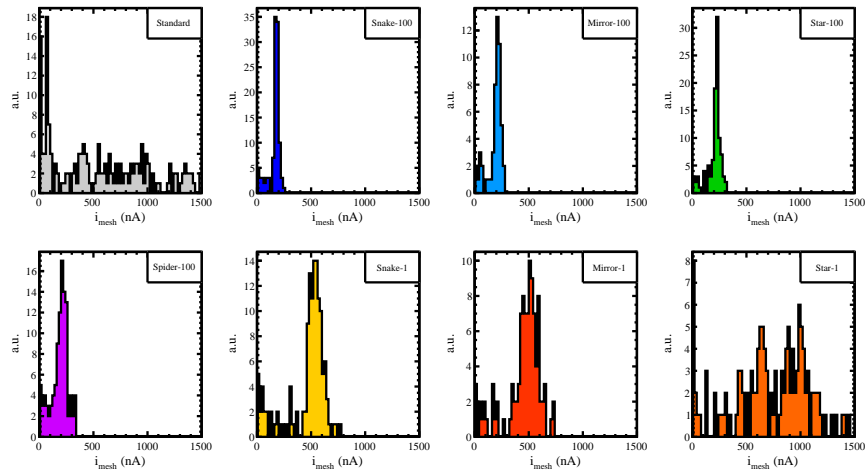


Figure 15: Mesh current at high pion rate in the H4 SPS beam line at CERN.

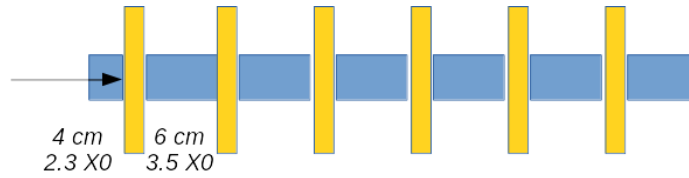


Figure 16: Sketch of the small calorimeter. Iron absorbers and Micromegas prototypes are colored in blue and yellow respectively. The arrow indicates the direction of the beam.

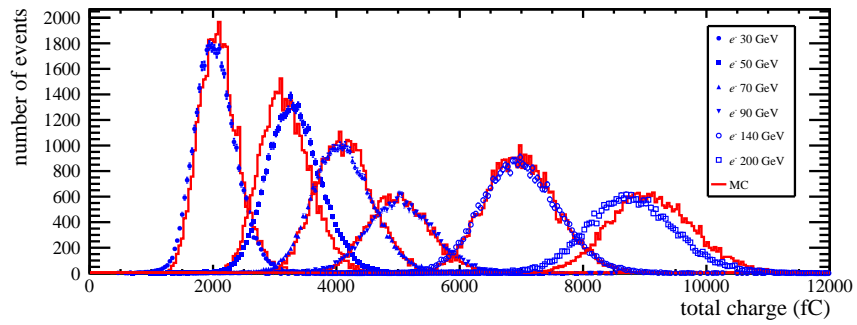


Figure 17: Total charge from electrons showering in a small sampling Micromegas calorimeter. Different markers indicate different energy of the beam. Simulation results are plotted as red histograms.

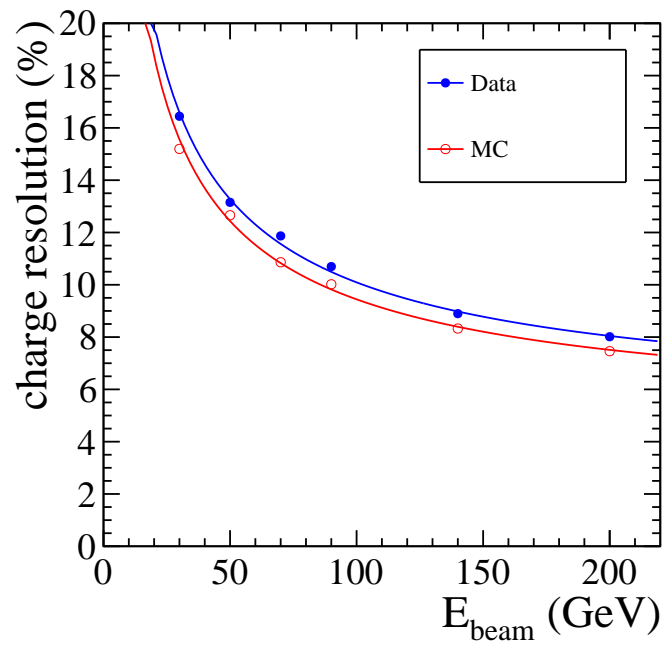
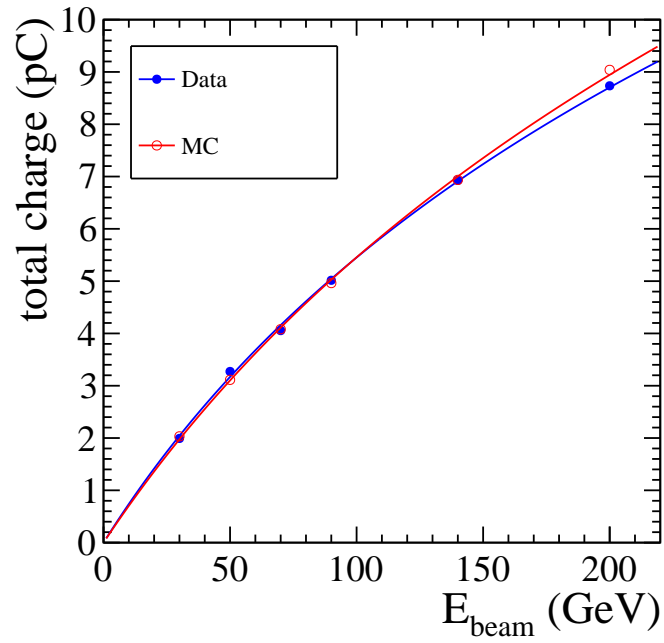


Figure 18: Electron response (top) and charge fluctuations (bottom) of a small sampling Micromegas calorimeter.

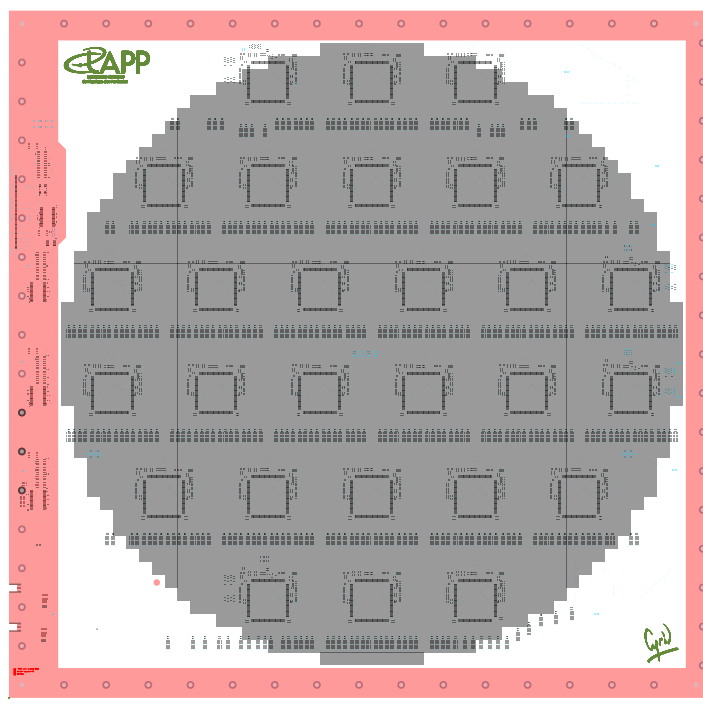


Figure 19: ASU design with 28 ASICs represented as black squares and 1792 pads forming a circular active area (drawn in in grey). The red perimeter is used for mechanical assembly, powering and connection to the readout.

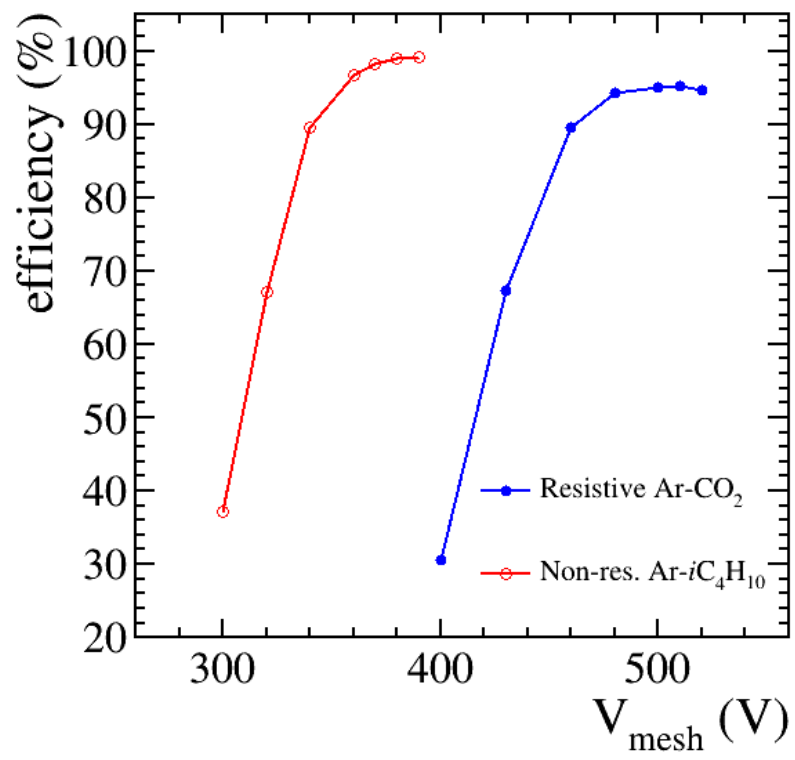


Figure 20: Muon efficiency using resistive and non-resistive ASUs and a different gas mixture).

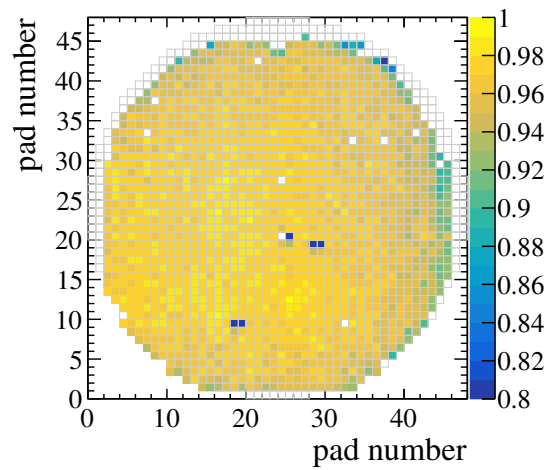
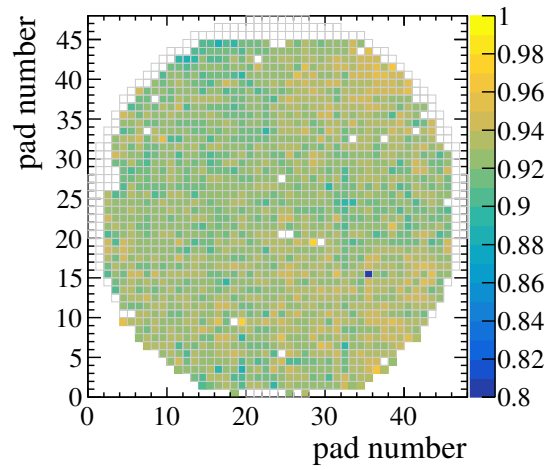
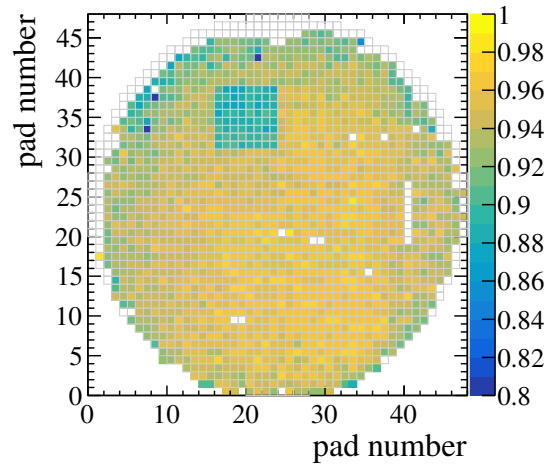


Figure 21: Efficiency maps of the three resistive ASU operated at 500 V.

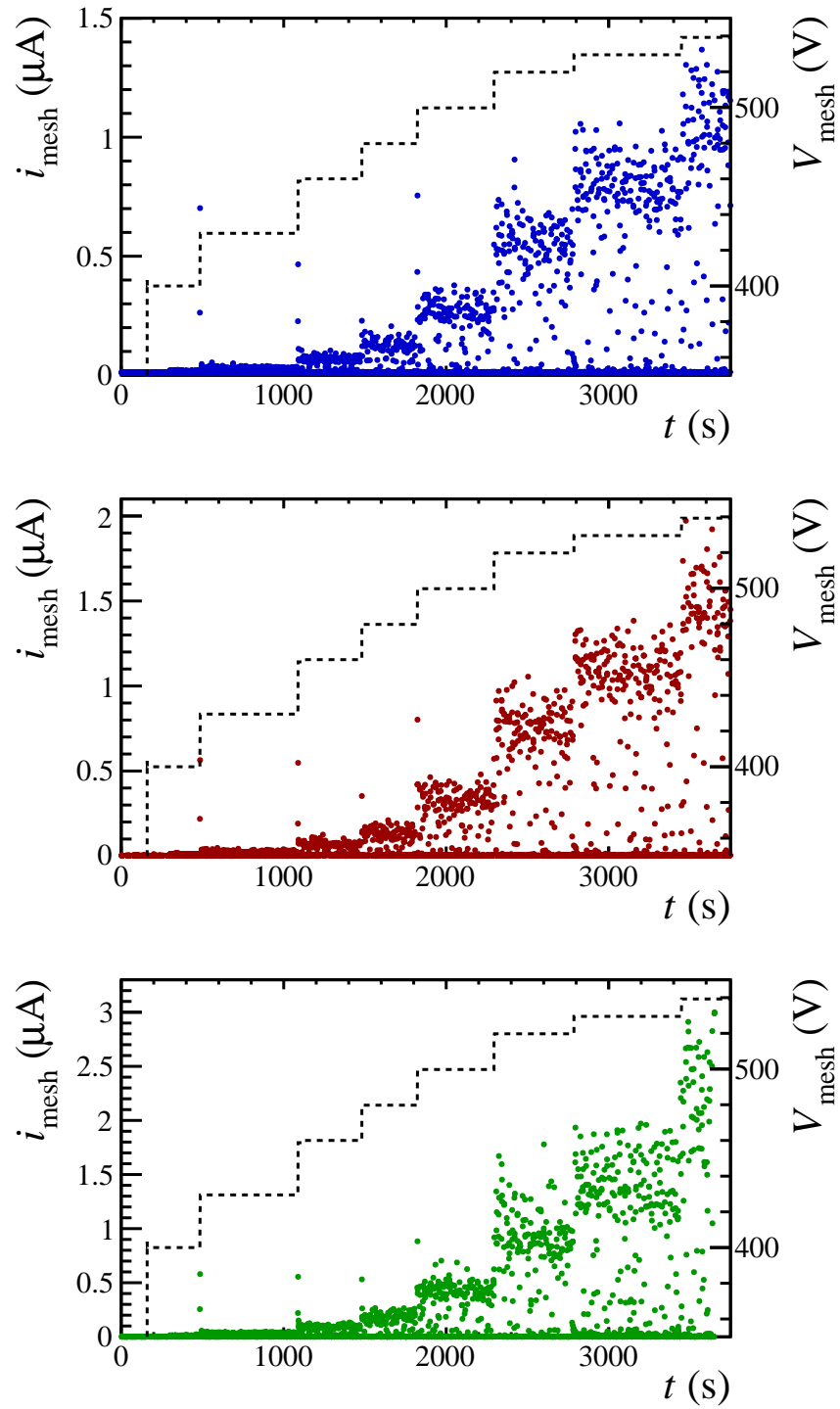


Figure 22: Mesh current during intense pion irradiation at increasing mesh voltages. The most upstream (downstream) prototype on the beam line is plotted at the top (bottom). Colored points stand for measured mesh currents and reflect the time structure of the pion spills, dashed lines indicate voltage settings.